

Synthesis, characterisation, and feasibility studies on the use of vanadium tellurate (VI) as a cathode material for aqueous rechargeable Zn-ion aqueous batteries

Received 00th January 20xx,
Accepted 00th January 20xx

DOI: 10.1039/x0xx00000x

Mangayarkarasi Nagarathinam^a, Cindy Soares^a, Yue Chen^b, Valerie Seymour^a, Vlastimil Mazanek^c, Zdenek Sofer^c, Oleg Kolosov^b, John Griffin^a, and Nuria Tapia-Ruiz^{a,†}

Aqueous rechargeable zinc-ion batteries (AZIBs) have drawn enormous attention in stationary applications due to their high safety and low cost. However, the search for new positive electrode materials with satisfactory electrochemical performance for practical applications remains a challenge. In this work, we report a comprehensive study on the use of the vanadium tellurate $(\text{NH}_4)_4\{(\text{VO}_2)_2[\text{Te}_2\text{O}_8(\text{OH})_2]\} \cdot 2\text{H}_2\text{O}$, which is tested for the first time as a cathode material in AZIBs.

1. Introduction

Rechargeable aqueous zinc-ion batteries (AZIBs) are a promising alternative to lead-acid batteries in grid energy storage systems.^{1–4} This is owing to the unique properties of Zn, which include a two-electron redox reaction, high theoretical gravimetric capacity (820 mAh g^{-1}), low redox potential (-0.76 V vs. standard hydrogen electrode (SHE)), low cost and abundance.^{5,6} Furthermore, AZIBs are risk-free and easier to scale up than the *classic* alkali-ion batteries, due to their non-toxicity, the use of a highly stable Zn metal anode, and non-flammable and non-volatile aqueous electrolytes.^{7–10} Nevertheless, the success of this technology remains a challenge, as AZIBs require high demanding conditions such as multivalent electrode materials with large interlayer space and robust architectures to withstand the huge stress imparted upon reversible solvated Zn^{2+} ion extraction.^{7,9} To date, significant efforts have been made to develop new manganese and vanadium-based cathode materials, where the latter have demonstrated impressively high capacities ($\sim 300 \text{ mAh g}^{-1}$),^{9,11–15} superior rate performance and prolonged cycle life, albeit with low operation voltages. In the pursuit of finding alternative vanadium-based electrode systems with improved electrochemical properties in AZIBs, we have investigated the use of $(\text{NH}_4)_4(\text{VO}_2)_2\text{Te}_2\text{O}_8(\text{OH})_2 \cdot 2\text{H}_2\text{O}$ as an electrode material, here abbreviated as VTe, which was first synthesised hydrothermally at $150 \text{ }^\circ\text{C}$ for 3 days by Hyejin et al. more than a decade ago.¹⁶ VTe consists of 1D infinite anionic $\{[\text{VO}_2]_2[\text{Te}_2\text{O}_8(\text{OH})_2]\}^{4-}$ chains separated by NH_4^+ cations and H_2O molecules, which act as strong pillars to keep structural

integrity (Fig. 1a). Electrode materials with polyanionic groups such as phosphates, silicates and sulfates have been reported to have higher electrochemical potential and improved thermal stability than their corresponding oxide counterparts.^{17,18} Thus, we will investigate the inductive and resonance effect of the polyanionic moiety $[\text{Te}_2\text{O}_8(\text{OH})_2]^{6-}$ in the redox potential of the vanadium oxide system and explore the redox activity of the Te ions upon Zn^{2+} ion insertion/extraction. This is the first example of a vanadium tellurate (VI) compound synthesised at room temperature and tested as a cathode in AZIBs, only preceded by studies on the high-voltage $\text{K}_2\text{Ni}_2\text{TeO}_6$ cathode used in potassium-ion batteries,¹⁹ and $\text{Na}_2\text{M}_2\text{TeO}_6$ compounds (M = Ni, Co, Zn, Mg), which showed high ionic conductivities ($4\text{--}11 \text{ Sm}^{-1}$) at $300 \text{ }^\circ\text{C}$.^{20,21}

2. Experimental Section

2.1 Synthesis of VTe

V_2O_5 (0.270 g, 1.5 mmol) and H_6TeO_6 (0.690 g, 3.0 mmol) were added to 10 ml of H_2O and stirred in a beaker until a homogeneous mixture was achieved. Then, 0.42 ml of 35 % NH_4OH solution was added dropwise with constant stirring to this solution. The yellow-orange reaction mixture was heated at $80 \text{ }^\circ\text{C}$ for 2–3 min until a clear solution was observed. Then, the reaction mixture was stirred at room temperature for 24 h and the solution was filtered to obtain a yellow precipitate. The yellow precipitate was washed with water and then dried at $60 \text{ }^\circ\text{C}$ under vacuum (0.850 g, 82% yield). All the chemicals were used as received from Sigma Aldrich without further purification. All the solvents used were of reagent grade.

2.2 Characterisation

Powder X-ray diffraction (PXRD) data were collected at ambient temperature using a Rigaku Smartlab X-ray diffractometer with a 9 kW Cu source generator ($\lambda_{\text{K}\alpha 1} = 1.54051 \text{ \AA}$) equipped with a high-resolution Vertical θ/θ 4-Circle Goniometer and a D/teX-

^a Department of Chemistry, Lancaster University, LA1 4YB, UK

^b Department of Physics, Lancaster University, LA1 4YB, UK.

^c Department of Inorganic Chemistry, University of Chemistry and Technology Prague, Technická 5, 166 28 Prague 6, Czech Republic.

† Corresponding author: n.tapia.ruiz@lancaster.ac.uk.

Electronic Supplementary Information (ESI) available: [details of any supplementary information available should be included here]. See DOI: 10.1039/x0xx00000x

ULTRA 250 high-speed position sensitive detector system. PXRD data were refined by the Rietveld refinement method using the TOPAS R2-1 software program.²²

Fourier transform infrared (FTIR) spectra were collected in the 400–4000 cm^{-1} range with a resolution of 8 cm^{-1} using a Shimadzu IRTracer-100 FTIR spectrophotometer. Spectra were collected as the sum of 36 scans. Samples were prepared by mixing the sample powders with KBr (Sigma Aldrich, 99%) using an agate mortar and pestle and then pressing the mixture into pellets at 5 tonnes cm^{-2} .

Elemental analysis was carried out on a Vario MICRO Cube instrument in CHNS analysis mode with a program designed for measuring 2 mg samples. For the measurement, samples were weighed directly into Sn boats using a high-precision balance. Oxygen was injected into the sample for 70 s and He was used as a carrier gas. The system was zeroed by running blank samples and then it was subsequently calibrated using a sulfanilamide ($\text{C}_6\text{H}_8\text{N}_2\text{O}_2\text{S}$) standard. Elemental analysis data for $\text{H}_{22}\text{N}_4\text{O}_{16}\text{Te}_2\text{V}_2$ (%): Theoretical: H 3.21, N 8.11. Experimental: H 3.31; N 8.05.

Thermogravimetric analyses (TGA) were carried out using a Thermys Analyzer (Setaram) with a DTA protected sensor. The sample was placed in an alumina crucible and was heated from room temperature to 700 °C in an argon atmosphere at a heating rate of 10 °C/min.

The microstructure of the samples was analysed using field emission scanning electron microscopy (FESEM), where the images were acquired using a JEOL JSM-7800F operating at 10.0 kV. Elemental analysis was performed at 12.0 kV using an X-ray Energy Dispersive Spectrometer (EDS) (X-Max50, large area 50 mm^2 Silicon Drift Detector (SDD) from Oxford Instruments). Samples were placed onto carbon tabs (G3348N, Agar Scientific) attached to the metal holder and coated with a thin layer of gold using a Quorum Q150RES sputter coater (Quorum Technologies Ltd) to increase their conductivity.

Transmission electron microscopy (TEM) images and single area electron diffraction (SAED) patterns were obtained using an EFTEM 2200 FS microscope (JEOL). A 200 keV acceleration voltage was used for the TEM data collection. Sample preparation was attained by drop-casting the suspension (1 mg ml^{-1} in water) on a TEM grid (Cu; 200 mesh; Formvar/carbon) and then drying it at 60 °C for 12 h.

^1H and ^{15}N solid-state NMR spectra were obtained at 16.4 T on a Bruker Avance III spectrometer operating at Larmor frequencies of 700.1 and 71.0 MHz, respectively. For ^1H experiments, powdered samples were dried at 100 °C under vacuum for 24 h and packed into 2.5 mm rotors and spun at 30 kHz. For ^{15}N experiments, powdered samples were packed into 4 mm rotors and spun at 12.5 kHz. ^1H spectra were acquired using a DEPTH pulse sequence to remove the background signal, with a recycle interval of 10 s. ^{15}N spectra were acquired using cross polarisation from ^1H . ^{125}Te solid-state NMR spectra were

obtained at 9.4 T on a Bruker Avance III 400 MHz spectrometer operating at a Larmor frequency of 126.2 MHz. Powdered samples were packed into 4 mm rotors and spun at 14 kHz. ^{125}Te spectra were acquired using a single 90° pulse with a repeat interval of 360 s. Spectra were referenced via secondary solid references of alanine (NH_3 $\delta_{\text{iso}} = 8.5$ ppm), glycine (NH_3 $\delta_{\text{iso}} = 347.4$ ppm), and $\text{Te}(\text{OH})_6$ (higher frequency peak $\delta_{\text{iso}} 692.2$ ppm) for ^1H , ^{15}N and ^{125}Te , respectively.

^1H chemical shifts were calculated using density functional theory (DFT). A calculation was carried out on the $(\text{NH}_4)_4\{(\text{VO}_2)_2[\text{Te}_2\text{O}_8(\text{OH})_2]\cdot 2\text{H}_2\text{O}$ crystal structure (ICSD 416841) using the CASTEP code. The structure was fully geometry optimised before calculation of the NMR parameters, using the GIPAW formalism²³ as implemented within CASTEP.^{24,25} Chemical shieldings were referenced via a separate calculation on *L*-alanine (reference shielding = 30.5 ppm). Calculated ^1H chemical shifts are shown in Table S1. Chemical shifts for crystallographically-distinct protons within H_2O molecules and NH_4^+ ions are averaged under the assumption of fast dynamic exchange between these positions.

2.3 Electrochemical tests

To fabricate the working electrodes, active material, super P carbon black and binder (Kynar 2801) in the weight ratio of 70:20:10 were thoroughly mixed with an agate mortar and pestle. The powdered mixture was then added to a vial and a few ml of *N*-methyl-2-pyrrolidone (NMP) were added to the mixture to make an electrode slurry. The slurry was stirred for 8 h at room temperature. 1.5 cm diameter electrodes with a thickness of 20 μm were prepared by casting the slurry onto Ti foil (used as a current collector) using the doctor-blade technique and punching the electrode-coated foil with a heavy-duty manual puncher. The mass loading of the active material was typically 2–3 mg cm^{-2} .

The electrochemical properties of VTe were evaluated using CR2032 stainless steel coin cells. Zn metal (180 μm thickness) was used as the counter and the reference electrode, glass microfiber filter (GB-100R, Whatman) as the separator, and a 3M $\text{ZnSO}_4\cdot 7\text{H}_2\text{O}$ aqueous solution as the electrolyte. Coin cells were aged at room temperature for 6 h before data collection took place. Galvanostatic charge/discharge cycling at a constant current in the voltage window of 0.4–1.4 V vs. Zn^{2+}/Zn was carried out using a Neware battery cycler (current range: 1–10 mA). Cyclic voltammetry (CV) data were collected at room temperature using an Iviumstat instrument (Ivium, Alvatek). Data were collected using a scan rate of 0.2 mV s^{-1} in the voltage window of 0.4–1.4 V vs. Zn^{2+}/Zn .

For the preparation of the concentric cells, VTe half-cells were discharged to 0.2 V to insert Zn^{2+} ions in the VTe electrode. The electrodes were removed in an open atmosphere from the discharged cells, paired immediately with a fresh VTe electrode and assembled in a CR2032 coin cell using a glass microfiber filter as the separator and an aqueous 3M ZnSO_4 solution as the electrolyte. The mass of the electrodes of the two cells was kept

similar and the specific capacity is calculated using the fresh VTe electrode. Galvanostatic charge/discharge cycling of the concentric cells at a constant current of 10 mA g⁻¹ in the voltage range of -1.7-1.5 V was carried out at room temperature using an Iviumstat instrument (Ivium, Alvatek). The concentric cell has an open-circuit voltage of -0.411 V and it is initially charged to 1.5 V and then discharged to -1.7 V continuously.

2.4 Ex situ X-ray photoelectron spectroscopy

X-ray photoelectron spectroscopy (XPS) data on ex situ samples were acquired using a Kratos Axis SUPRA using monochromated Al K α (1486.69 eV) X-rays at 15 mA emission and 12 kV HT (180W) and a spot size/analysis area of 700 x 300 μ m. The instrument was calibrated to gold metal Au 4f (83.95 eV) and dispersion adjusted to give a binding energy of 932.6 eV for the Cu 2p_{3/2} line of metallic copper. Ag 3d_{5/2} line FWHM at 10 eV pass energy was 0.544 eV. Source resolution for monochromatic Al K α X-rays is \sim 0.3 eV. The instrumental resolution was determined to be 0.29 eV at 10 eV pass energy using the Fermi edge of the valence band for metallic silver. Resolution with charge compensation system on < 1.33 eV FWHM on PTFE. High-resolution spectra were obtained using a pass energy of 20 eV, step size of 0.1 eV and sweep time of 60s, resulting in a line width of 0.696 eV for Au 4f^{7/2}. Survey spectra were obtained using a pass energy of 160 eV. Charge neutralisation was achieved using an electron flood gun with filament current = 0.38 A, charge balance = 2 V, filament bias = 4.2 V. Successful neutralisation was adjudged by analysing the C 1s region wherein a sharp peak with no lower BE structure was obtained. Spectra have been charge corrected to the main line of the carbon 1s spectrum (adventitious carbon) set to 284.8 eV. All data was recorded at a base pressure of below 9 x 10⁻⁹ Torr and a room temperature of 294 K. Data was analysed using CasaXPS v2.3.19PR1.0. Peaks were fit with a Shirley background before component analysis.²⁶ The samples were transferred from the glovebox using a custom vacuum sealed transfer arm.

2.5 Quartz crystal microbalance experiments

Quartz crystal microbalance (QCM) experiments were performed on an eQCM10 quartz crystal microbalance (GAMRY). Electrodes were prepared by coating an Au-coated quartz crystal (QCM5140CrAu120-050-Q, 5 MHz, 14 mm sensor diameter, 12 mm front/5 mm back electrode diameter) with a mixture of the VTe powder (active material), super P carbon (conductive agent), and Polyvinylidene difluoride (PVDF, binder) in a weight ratio of 58:17:25. Then, the electrode was heated at 60 °C for 24 h. The thickness of the composite electrode was *ca.* 20 μ m. Operando EQCM was conducted during cyclic voltammetry tests. The mass change of the VTe-coated QCM electrode, Δm , was calculated from the change in resonance frequency (Δf), using the Sauerbrey equation (1):

$$\Delta m = \left(\frac{A \sqrt{\rho_q \mu_q}}{2 f_0^2} \right) \Delta f \quad (1)$$

where f_0 is the resonance frequency of the QCM electrode before the electrochemical tests, A is the active area of the QCM electrode (0.205 cm²), ρ_q is the density of quartz (2.648 g cm⁻³), and μ_q is the shear modulus of quartz (2.947 x 10¹¹ g cm⁻¹ s⁻²).²⁷

The molar number of electrons participate in the charge transfer (N) are

$$N = \frac{n \Delta m}{M_w} = \frac{\Delta C}{F} \quad (2)$$

where ΔC is the charge passed during electrolysis, M_w is the molecular weight, F is Faraday's constant, 96485 C mol⁻¹ and n is the valence number of Zn.

Equation (2) can be then written as:

$$\left| \frac{\Delta m}{\Delta C} \right| = \frac{M_w}{F n} \quad (3)$$

By plotting the Δm vs. ΔC , the molecular weight of the exchanged ion can be calculated from the slope value according to the equation (3).

2.6 Post-mortem studies

For post-mortem studies, electrodes were electrochemically cycled at different states of charge and then coin cells were disassembled and the electrodes washed with deionised water a few times under a steady flow of nitrogen gas. Electrodes were transferred immediately to a glovebox antechamber which was first flushed with Ar gas 5 times and then dried under vacuum at room temperature. For XPS measurements, electrodes were packed in the glovebox under Ar atmosphere. Electrodes were in contact with air during PXRD, FTIR and, FESEM data collection.

3. Results and discussion

(NH₄)₄{(VO₂)₂[Te₂O₈(OH)₂]} · 2H₂O (VTe), was obtained using a modified synthetic procedure from the literature (see Experimental Section).¹⁶ Rietveld analysis on the XRD data shows that the structure crystallises in a monoclinic $P2_1/n$ space group with $a = 7.37(1)$ Å, $b = 17.12(2)$ Å and $c = 7.37(1)$ Å, $\beta = 118.70(3)$ °, in agreement with the literature (Fig. 1b).¹⁶ The structure of VTe consists of 1D infinite anionic [(VO₂)₂[Te₂O₈(OH)₂]]⁴⁻ chains along the c direction with edge-shared VO₆ and TeO₅(OH) octahedral units that form V₂O₁₀ and Te₂O₈(OH)₂ dimers. These chains are connected by an extended hydrogen network of N-H...O and O-H...O bonds (originated by the presence of NH₄⁺ cations and H₂O molecules in the structure), and O-H...O hydrogen bonds from the OH group of the TeO₅(OH) dimers (Fig. 1a). No impurities were observed in the diffraction data.

The large interlayer spacing of 8.6 Å in VTe allows a rapid migration of Zn²⁺ ions along the ac plane. The intralayer spacing compares well to other ammonium vanadate systems with excellent electrochemical performance due to their large ion diffusion channels, such as NH₄V₄O₁₀ and (NH₄)_{0.5}V₂O₅.^{28,29} Elemental analysis confirmed the percentage of nitrogen and

hydrogen as in the proposed molecular formula for VTe (see Experimental Section), while EDX analysis confirms that the V:Te and V:N elemental ratio is nearly equal to 1:1 and 1:2, respectively (Fig. S1). Thermogravimetric analysis data shows a mass loss of 23.4% between R.T. and 410 °C, which agrees with the removal of all the H₂O and NH₃ molecules in the compound (Fig. S2). SEM/TEM images in Fig. 1c and d) show that the VTe sample consists of 200–500 nm platelets. The TEM image in Fig. 1d shows that the platelets have smooth edges, and its corresponding ring-like SAED pattern (Fig. S3) shows the polycrystalline nature of the sample. The ¹H MAS NMR spectrum of VTe shows three main resonances at 10, 7 and 5 ppm. Based on their relative intensities and chemical shifts, these are attributed to OH groups, pillared NH₄⁺ ions and H₂O molecules, respectively (Fig. 1e). DFT calculations on the published crystal structure¹⁶ support this assignment (Fig. 1e). The OH resonance is slightly broader than the NH₄⁺ and H₂O resonances owing to stronger dipolar interactions which reduces its apparent intensity in the experimental spectrum.

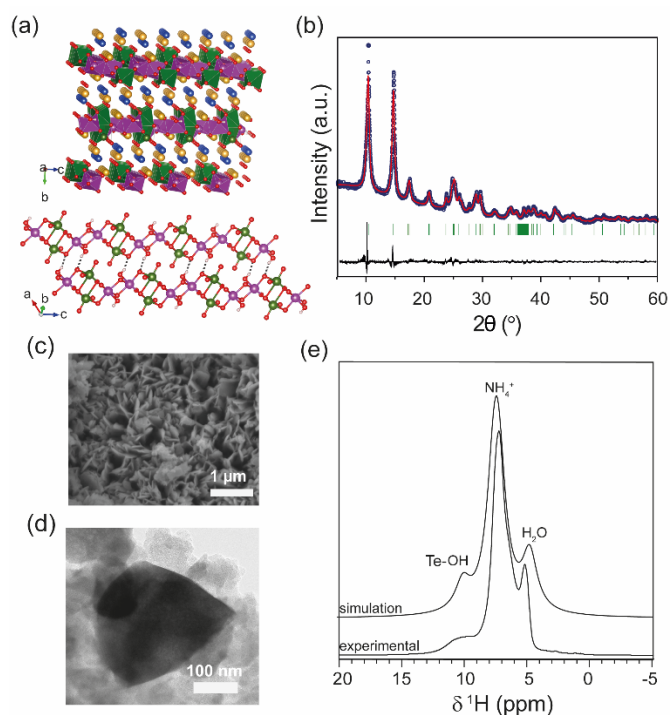


Fig. 1. (a) Crystal structure of layered VTe. H atoms of H₂O (blue) and NH₄⁺ (yellow) molecules are omitted for clarity; and $\{[VO_2]_2[Te_2O_8(OH)_2]\}^{4-}$ anionic chains linked by Te-O-H \cdots O-Te bonds along the *ac* plane. O-H \cdots O bonds are shown as dotted lines and NH₄⁺ and water molecules are removed for clarity. V/VO₆ polyhedra (green), Te/TeO₆ polyhedra (pink) and O (red). (b) Experimental powder XRD data of the as-synthesized VTe product. The observed data (blue), calculated data using the Rietveld method (red), difference between experimental and calculated profiles (black) and Bragg positions (green vertical bars) are shown. (c) FESEM image of VTe (d) TEM image of VTe and (e) DFT simulated and experimental ¹H MAS NMR spectra of VTe.

The ¹⁵N MAS NMR spectrum for the pristine material shows a single peak at −357 ppm, which contrasts with the two crystallographic NH₄⁺ environments in the crystal structure (Fig. S4). DFT calculations predict a small chemical shift difference of 6 ppm between the two N sites, which is less than the ~ 8 ppm

linewidth in the experimental spectrum. This explains the inability to distinguish between these two sites. The ¹²⁵Te MAS NMR spectrum shows two distinct resonances of similar intensity at 765 and 740 ppm (Fig. S5). This is inconsistent with the published crystal structure, which shows a single Te site. An explanation for this might be a small break in the symmetry of VTe due to the loss of H₂O molecules.

Electrochemical studies were conducted to assess the performance of VTe as a cathode material in AZIBs. CV data depict a multistep insertion/extraction of Zn²⁺ ions, where the first scan shows cathodic peaks at 1.04 and 0.59 V and anodic peaks at 0.75, 1.06 and 1.23 V, which correspond to reversible reactions involving V⁵⁺/V⁴⁺ and V⁴⁺/V³⁺ redox couples (Fig. 2a). These peaks were assigned by direct comparison to other vanadate systems.^{28,30} Peaks at 1.06 and 1.23 V are attributed to the extraction of Zn²⁺ ions from energetically different crystallographic sites.³¹ GC data shows three discharge plateaus at *ca.* 0.90 V, 0.57 V and 0.49 V, totalling a capacity of 287 mAh g⁻¹ (Fig. 2b, and magnified view in Fig. S6). Upon charge, the capacity cannot be fully retrieved (232 mAh g⁻¹), due to the irreversible nature of the lowest voltage plateau. This corresponds to an initial Coulombic efficiency (CE) of *ca.* 80%. A progressive capacity decay occurs with increasing cycle number, leading to a discharge capacity of 141 mAh g⁻¹ in the 20th cycle (Fig. S7). GC tests were run using different voltage windows to optimise the long-term cycling stability of VTe without any further improvement on the cycling stability (Fig. S8). Furthermore, rate capability studies in the 0.4–1.2 V voltage window using a current rate in the 10–340 mA g⁻¹ current range are shown in Fig. S9. Although the performance of VTe was not remarkable at high rates, several approaches previously used with other Zn cathodes might be followed to improve Zn²⁺ insertion/extraction kinetics, *e.g.*, mixing VTe with conducting carbon-based materials.^{32,33} This work, however, falls outside the remit of the work presented here.

Electrochemical tests using concentric (VTe||3 M ZnSO₄ aq.||Zn_xVTe) cells (Fig. 2c) were run to disregard parasitic reactions arising from the use of Zn as a counter electrode, *e.g.*, uncontrolled dendrite formation and Zn passivation, which could be the cause for the capacity decay observed in Zn half-cells.³⁴ Load curves showed well-defined, long, and reversible voltage plateaus at *ca.* 0.5 and −0.5 V upon charge and discharge, respectively. The charge capacity increased from 219 to 258 mAh g⁻¹ from the first to the second cycle, while the discharge capacity remained the same (271 mAh g⁻¹). A reversible discharge capacity of 251 mAh g⁻¹ was observed after 20 cycles, which corresponds to an excellent capacity retention of 91% (Fig. 2d). These results contrast with the poorer capacity retention observed for VTe in the Zn half-cell after 20 cycles (*i.e.*, 61%) (Fig. S7), which might be attributed to particle agglomeration, as observed in the FE-SEM images shown in Fig. S10. Despite the good capacity retention, a large voltage hysteresis was observed between the charge and discharge plateau (Fig. 2c). We attribute this large voltage hysteresis to high energetics/structural re-ordering occurring in the material, and slow kinetics during Zn²⁺ ion (de)insertion.³⁵ This may be reduced by optimising the electrolyte solution, tailoring the

crystal size, morphology, and carbon coating of the material, among others.^{36,37}

Zn 2p XPS spectrum of the electrode after 6 h under rest conditions (OCV) confirmed the presence of Zn²⁺ ions by showing two asymmetric peaks with binding energies of 1021.5 eV and 1044.6 eV, assigned to Zn 2p_{3/2} and Zn 2p_{1/2} core levels, respectively (Fig. 3a). Furthermore, the N1s XPS spectrum showed a drastic decrease in the intensity of the N1s peak (centred at 401.77 eV in the pristine electrode and indicative of the presence of NH₄⁺ ions) which confirmed that almost all the NH₄⁺ ions acting as pillars between the {[VO₂]₂[Te₂O₈(OH)₂]}⁴⁻ chains are removed at this stage (Fig. S11). Nevertheless, it needs to be noted that XPS is a surface analysis technique and that some NH₄⁺ ions could have been trapped in the bulk structure. Therefore, these data demonstrate that VTe is not completely stable in contact with the 3M ZnSO₄ aqueous mild electrolyte solution and that some pre-intercalation of Zn²⁺ ions takes place before applying current. Charge neutrality is then achieved by the reduction of V⁵⁺ ions to V⁴⁺, as observed in the V-2p XPS spectrum (Fig. 3b), where two peaks with maxima at 517.4 and 516.3 eV that correspond to the coexistence of V⁵⁺ and V⁴⁺ oxidation states were observed.

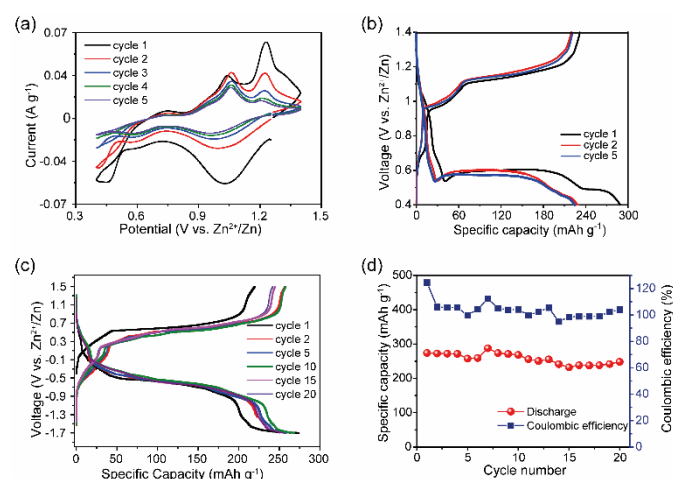


Fig. 2. (a) CV data of VTe in the 0.4–1.4 V vs. Zn²⁺/Zn voltage range, and using a 0.2 mV s⁻¹ scan rate. (b) Galvanostatic charge-discharge data of VTe in Zn half-cells in the 0.4–1.4 V vs. Zn²⁺/Zn voltage range using a current density of 10 mA g⁻¹. (c) Galvanostatic charge-discharge profiles of concentric (VTe||3 M ZnSO₄ aq. ||Zn₂VTe) cells in the -1.7–1.5 V voltage range at a current density of 10 mA g⁻¹ during the 1st, 2nd, 5th, 10th, 15th, and 20th cycles; and (d) Specific capacity vs. Cycle number plot with Coulombic efficiencies over 20 cycles for concentric (VTe||3 M ZnSO₄ aq. ||Zn₂VTe) cells.

By contrast, the V-2p XPS spectrum of the pristine electrode shows a single V 2p_{3/2} peak with a binding energy of 517.5 eV and a broader V 2p_{1/2} spin-orbit pair at higher binding energy, *i.e.*, 524.9 eV, which are typical for V⁵⁺ ions in oxides.^{6,38,39}

Preliminary operando EQCM studies were conducted to identify active charge carriers during Zn²⁺ ion intercalation (Fig. 3d, Fig. S12 and Table S2). During the initial stages of discharge (Region I), the mass change per charge transfer ($\Delta m/e$) fits with the theoretical capacity value of ca. 1.1 Zn²⁺ (347.89 $\mu\text{g C}^{-1}$), implying that Zn²⁺ ions are inserted in their non-hydrated form. This matches with the cathodic peak observed in the CV data for the reduction of V⁵⁺ ions to V⁴⁺ (Fig. 2a). Region 2, which coincides

with the second cathodic peak related to the further reduction of V⁴⁺ ions to V³⁺, corresponds to a total charge value of 309 $\mu\text{g C}^{-1}$, equivalent to the insertion of 0.9 Zn²⁺ ions. During charge, the reverse process occurs, showing extraction of only one Zn²⁺ based on the $\Delta m/e$ value measured (292 $\mu\text{g C}^{-1}$), in agreement with the Zn 2p XPS spectrum, which shows that there are remaining Zn²⁺ ions upon charge (Fig. 3a) and that all V³⁺ ions have been oxidised to mixed valent V⁴⁺ and V⁵⁺ (Fig. 3b).

N1s XPS spectra of the fully discharged and charged electrodes showed that the removal of NH₄⁺ ions was irreversible upon Zn²⁺ intercalation (Fig. S11). Similar behaviour was reported in (NH₄)₂V₆O₁₆ · 0.9H₂O, where it was noted that Zn²⁺ insertion irreversibly displaced the NH₄⁺ ions from the structure.⁴⁰ FTIR data agree with the XPS data, showing a broad peak at about 3153 cm⁻¹ corresponding to the N-H asymmetric stretching mode of the NH₄⁺ ions, which is no longer present at the OCV, discharge and charged state spectral data (Fig. S13).⁴⁰

Upon discharge to 0.5 V, the Zn 2p peaks present in the Zn-2p spectrum of the OCV sample shifted to lower binding energies (Fig. 3a). This is explained with a more covalent environment than that in the OCV state. Concomitant to the insertion of Zn²⁺ ions into VTe, we observed a reduction of the V⁵⁺/V⁴⁺ redox couple to V⁵⁺/V⁴⁺/V³⁺, which explained the broadening and shift toward lower binding energies of the V 2p_{3/2} and V 2p_{1/2} peaks in the V-2p XPS spectrum (Fig. 3b).^{6,38,39} Furthermore, EDX data showed a qualitative increase in Zn²⁺ ions in the discharged state compared to the charged state (Table S3). The extra discharge capacity observed in the galvanostatic data might be accounted for the irreversible formation of insulating by-products such as zinc hydroxide sulfate (ZHS) salts at the electrode surface due to electrolyte decomposition.^{41,42} IR spectrum of the discharged sample showed strong peaks at 1055 and 1116 cm⁻¹, typically attributed to the S-O stretching bands of SO₄²⁻ moieties in the sample (Fig. S13).⁴³

After charging to 1.4 V, we observed that the Zn 2p_{3/2} and Zn 2p_{1/2} peaks do not fully disappear in the XPS spectrum due to incomplete removal of Zn²⁺ ions (Fig. 3a), confirming the low first coulombic efficiency observed in the galvanostatic data (Fig. 2b). The Zn 2p peaks showed lower binding energy to those observed in the discharged state which suggests weaker interactions between Zn²⁺ ions and the electrode host.⁶ Zn²⁺ ion extraction was followed by re-oxidation of the majority of the V⁴⁺ and V³⁺ ions to V⁵⁺, further confirming the reversible reactions involving the V⁵⁺/V⁴⁺ and V⁴⁺/V³⁺ redox couples observed in the CV data shown in Fig. 2a.

Te-3d XPS spectra of VTe at the pristine state showed two peaks at 576.9 eV and 587 eV corresponding to the Te-3d_{5/2} and Te 3d_{3/2} core levels, respectively, and characteristic of the binding energy of Te⁶⁺ ions (Fig. 3c).^{44–46} At the OCV state, we observed a shift of the two peaks to lower binding energy, which we attribute to different Te environments. For instance, Te⁶⁺ ions in Te(OH)₆ and TeO₃ have binding energies of 576.7 and 577.3 eV.^{45,47} Upon discharge, these peaks further shift to lower binding energies, *i.e.*, 576 and 586.4 eV and two additional peaks with maxima at 577.7 and 588.2 eV appear, which might be attributed to a change in the valence state of

Te⁶⁺ to Te⁴⁺.⁴⁸ Nevertheless, given the different forms in which Te⁶⁺ can be present, detailed research is required to unambiguously assigned those peaks to Te⁴⁺. At the fully charged state, the peaks associated with the Te-3d_{5/2} and Te3d_{3/2} return to the OCV state.

Ex situ XRD studies were performed on VTe electrodes at different charge states to understand the structural changes taking place during the first cycle (Fig. S14). From the PXRD data, one can observe structural changes occurring during the first discharge process, guided by the presence of diffraction peaks at 11.9°, 32.3° and 35.6° 2θ (marked with a star symbol). Attempts to model the structure of the fully reduced phase from the powder diffraction pattern were carried out using Expo2014 software.^{49,50} The best possible solution found yielded a phase with a monoclinic crystal structure and lattice parameters *a* = 9.67 Å, *b* = 7.44 Å and *c* = 4.66 Å; α, γ = 90° and β = 92.3°. No traces of crystalline impurities were observed in the PXRD data despite the presence of IR peaks originating from SO₄²⁻ ions (Fig. S13).

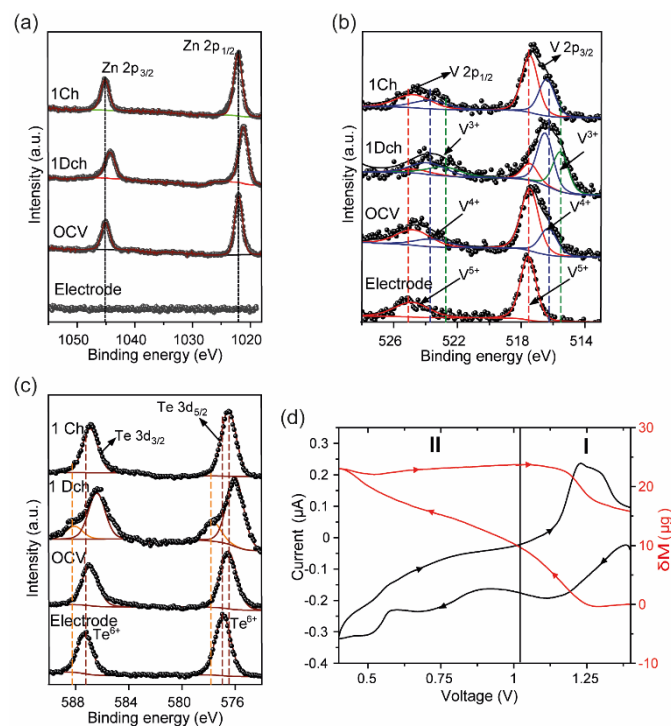
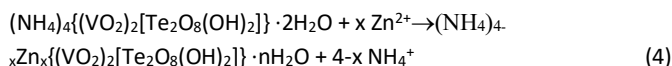


Fig. 3. (a) Normalised Zn-2p spectra, (b) V-2p XPS spectra, and (c) Te-3d XPS spectra of VTe at different states of charge. (d) EQCM and corresponding CV data of VTe-coated electrode vs. Zn²⁺/Zn at 0.1 mV s⁻¹ in 3M ZnSO₄ electrolyte solution. Electrode refers to the pristine electrode and OCV, 1Dch and 1Ch refer to the electrodes extracted from the cell after resting for 6h, 1st full discharge and charge cycles, respectively.

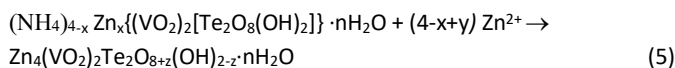
XRD data of the charged electrode shows a clear loss of crystallinity in the material, as reflected by the peak broadening observed in the diffraction pattern. Nevertheless, some of the diffraction peaks observed in the discharged product were still present, showing that the structure is kept after charge. A detailed diffraction study of the effects of Zn²⁺ insertion/extraction in this material is still required. Based on the above-mentioned experimental results, we propose that

the following reactions occur during OCV (Eq. 4), discharge (Eq. 5) and charge processes (Eq. 6):

Cathode at the OCV state:



Cathode during the first discharge:



Cathode during the first charge:



4. Conclusions

In conclusion, (NH₄)₄{(VO₂)₂[Te₂O₈(OH)₂]} · 2H₂O was first tested as a cathode material in AZIBs due to its vanadium redox centres and its large interlayer space, which enable Zn-ion insertion/extraction between the 1D {[VO₂]₂[Te₂O₈(OH)₂]}⁴⁻ chains. To the best of our knowledge, this is the first-ever reported vanadium tellurate (VI) tested as a positive electrode in AZIBs. The material shows a remarkable discharge capacity of ca. 283 mAh g⁻¹ in the 0.4–1.4 V vs. Zn²⁺/Zn voltage range, using a current density of 10 mA g⁻¹. Furthermore, in concentric cells, VTe shows excellent cycling stability, retaining about 91% of its initial discharge capacity after 20 cycles. Despite the promising results, improvements to the present work are under progress and include various strategies, including the optimisation of suitable electrolyte formulations, where the V⁵⁺ state remains stable and prevents the pre-insertion of Zn²⁺ ions, and cycling with a modified Zn anode in a half-cell. Nevertheless, we believe that these results provide great opportunities for the exploration of this material and related compounds as energy storage materials for AZIBs.

Conflicts of interest

There are no conflicts to declare.

Data access statement

All research data supporting this publication are directly available within the publication.

Acknowledgements

NTR is indebted to the Royal Society (RG170150), Energy Lancaster and Lancaster University for financial support. We are grateful to Dr Sara Baldock for assistance with SEM data collection, Dr Nathan Halcovitch for his help with elemental analysis and Dr David Rochester for ICP-OES measurements. XPS data collection was conducted by Mark Isaacs and performed at the EPSRC National Facility for XPS (“HarwellXPS”), operated by Cardiff University and UCL, under Contract No. PR16195. ZS

would like to thank the Czech Science Foundation (GACR No. 20-16124J) for financial support.

Notes and references

- 1 L. E. Blanc, D. Kundu and L. F. Nazar, *Joule*, 2020, **4**, 771–799.
- 2 B. Tang, L. Shan, S. Liang and J. Zhou, *Energy Environ. Sci.*, 2019, **12**, 3288–3304.
- 3 W. Xu and Y. Wang, *Nano-Micro Lett.*, 2019, **11**, 90.
- 4 K. Kordesh and M. Weissenbacher, *J. Power Sources*, 1994, **51**, 61–78.
- 5 C. Xu, B. Li, H. Du and F. Kang, *Angew. Chemie - Int. Ed.*, 2012, **51**, 933–935.
- 6 D. Kundu, B. D. Adams, V. Duffort, S. H. Vajargah and L. F. Nazar, *Nat. Energy*, 2016, **1**, 16119.
- 7 A. Konarov, N. Voronina, J. H. Jo, Z. Bakenov, Y.-K. Sun and S.-T. Myung, *ACS Energy Lett.*, 2018, **3**, 2620–2640.
- 8 X. Wang, Z. Zhang, B. Xi, W. Chen, Y. Jia, J. Feng and S. Xiong, *ACS Nano*, 2021, **15**, 9244–9272.
- 9 M. Song, H. Tan, D. Chao and H. J. Fan, *Adv. Funct. Mater.*, 2018, **28**, 1802564.
- 10 M. D. Slater, D. Kim, E. Lee and C. S. Johnson, *Adv. Funct. Mater.*, 2013, **23**, 947–958.
- 11 Y. Zhang, E. H. Ang, K. N. Dinh, K. Rui, H. Lin, J. Zhu and Q. Yan, *Mater. Chem. Front.*, 2021, **5**, 744–762.
- 12 N. Bensalah and Y. De Luna, *Energy Technol.*, 2021, **9**, 2100011.
- 13 L. Shan, Y. Wang, S. Liang, B. Tang, Y. Yang, Z. Wang, B. Lu and J. Zhou, *InfoMat*, 2021, **3**, 1028–1036.
- 14 Z. Liu, Y. Yang, S. Liang, B. Lu and J. Zhou, *Small Struct.*, 2021, **2**, 2100119.
- 15 I. Stoševski, A. Bonakdarpour, B. Fang, S. T. Voon and D. P. Wilkinson, *Int. J. Energy Res.*, 2021, **45**, 220–230.
- 16 K. Hyejin, C. Yoonsuk, Y. Hoseop and D. Junghwan, *Zeitschrift für Anorg. und Allg. Chemie*, 2007, **633**, 473–477.
- 17 C. Liu, Z. G. Neale and G. Cao, *Mater. Today*, 2016, **19**, 109–123.
- 18 C. Masquelier and L. Croguennec, *Chem. Rev.*, 2013, **113**, 6552–6591.
- 19 T. Masese, K. Yoshii, Y. Yamaguchi, T. Okumura, Z. D. Huang, M. Kato, K. Kubota, J. Furutani, Y. Orikasa, H. Senoh, H. Sakaebe and M. Shikano, *Nat. Commun.*, 2018, **9**, 3823.
- 20 M. A. Evstigneeva, V. B. Nalbandyan, A. A. Petrenko, B. S. Medvedev and A. A. Kataev, *Chem. Mater.*, 2011, **23**, 1174–1181.
- 21 K. Sau and P. P. Kumar, *J. Phys. Chem. C*, 2015, **119**, 1651–1658.
- 22 A. A. Coelho, *J. Appl. Crystallogr.*, 2018, **51**, 210–218.
- 23 C. J. Pickard and F. Mauri, *Phys. Rev. B - Condens. Matter Mater. Phys.*, 2001, **63**, 245101.
- 24 S. J. Clark, M. D. Segall, C. J. Pickard, P. J. Hasnip, M. I. J. Probert, K. Refson and M. C. Payne, *Zeitschrift für Krist.*, 2005, **220**, 567–570.
- 25 M. D. Segall, P. J. D. Lindan, M. J. Probert, C. J. Pickard, P. J. Hasnip, S. J. Clark and M. C. Payne, *J. Phys. Condens. Matter*, 2002, **14**, 2717–2744.
- 26 N. Fairley, V. Fernandez, M. Richard-Plouet, C. Guillot-Deudon, J. Walton, E. Smith, D. Flahaut, M. Greiner, M. Biesinger, S. Tougaard, D. Morgan and J. Baltrusaitis, *Appl. Surf. Sci. Adv.*, 2021, **5**, 100112.
- 27 G. Sauerbrey, *Zeitschrift für Phys.*, 1959, **155**, 206–222.
- 28 D. Bin, Y. Liu, B. Yang, J. Huang, X. Dong, X. Zhang, Y. Wang and Y. Xia, *ACS Appl. Mater. Interfaces*, 2019, **11**, 20796–20803.
- 29 C. Zhu, C. Wang, F. Liu, J. Zhou, S. Liang, B. Tang, A. Pan and G. Fang, *J. Mater. Chem. A*, 2018, **7**, 940–945.
- 30 B. Sambandam, V. Soundharajan, S. Kim, M. H. Alfaruqi, J. Jo, S. Kim, V. Mathew, Y. K. Sun and J. Kim, *J. Mater. Chem. A*, 2018, **6**, 3850–3856.
- 31 S. Islam, M. H. Alfaruqi, B. Sambandam, D. Y. Putro, S. Kim, J. Jo, S. Kim, V. Mathew and J. Kim, *Chem. Commun.*, 2019, 2–5.
- 32 C. Shen, X. Li, N. Li, K. Xie, J. G. Wang, X. Liu and B. Wei, *ACS Appl. Mater. Interfaces*, 2018, **10**, 25446–25453.
- 33 F. Tang, J. Gao, Q. Ruan, X. Wu, X. Wu, T. Zhang, Z. Liu, Y. Xiang, Z. He and X. Wu, *Electrochim. Acta*, 2020, **353**, 136570.
- 34 H. Jia, Z. Wang, B. Tawiah, Y. Wang, C. Y. Chan, B. Fei and F. Pan, *Nano Energy*, 2020, **70**, 104523.
- 35 W. Oh, H. Park, B.-S. Jin, R. Thangavel and W.-S. Yoon, *J. Mater. Chem. A*, 2020, **8**, 10331–10336.
- 36 H. Huang, S. C. Yin, T. Kerr, N. Taylor and L. F. Nazar, *Adv. Mater.*, 2002, **14**, 1525–1528.
- 37 H. S. Lee, V. Ramar, S. Kuppan, M. Nagarathinam, M. Law, C. Wang, A. Tripathi and P. Balaya, *Electrochim. Acta*, 2021, **372**, 137831.
- 38 T. Wei, Q. Li, G. Yang and C. Wang, *J. Mater. Chem. A*, 2018, **6**, 8006–8012.
- 39 Z. Li, S. Ganapathy, Y. Xu, Z. Zhou, M. Sarilar and M. Wagemaker, *Adv. Energy Mater.*, 2019, **9**, 1801819.
- 40 F. Hu, Y. Gu, F. Cui, G. Song and K. Zhu, *Chinese Chem. Lett.*, 2021, **32**, 3793–3798.
- 41 G. Yang, Q. Li, K. Ma, C. Hong and C. Wang, *J. Mater. Chem. A*, 2020, **8**, 8084–8095.
- 42 L. Zhang, X. Dai, X. Wang, J. Chen, Z. Niu and F. Wan, *Nat. Commun.*, 2018, **9**, 1656.
- 43 N. V. Chukanov, R. K. Rastsvetaeva, S. M. Aksenov, I. V. Pekov, D. I. Belakovskiy, G. Blass and G. Möhn, *Geol. Ore Depos.*, 2013, **55**, 663–668.
- 44 M. K. Bahl, R. L. Watson and K. J. Irgolic, *J. Chem. Phys.*, 1977, **66**, 5526–5535.
- 45 W. E. Swartz, K. J. Wynne and D. M. Hercules, *Anal. Chem.*, 1971, **43**, 1884–1887.
- 46 L. Y. Zhang and K. H. Lii, *Dalt. Trans.*, 2019, **48**, 15231–15235.
- 47 J. M. M. Millet, H. Roussel, A. Pigamo, J. L. Dubois and J. C. Jumas, *Appl. Catal. A Gen.*, 2002, **232**, 77–92.
- 48 D. Xiao, S. Wang, E. Wang, Y. Hou, Y. Li, C. Hu and L. Xu, *J. Solid State Chem.*, 2003, **176**, 159–164.
- 49 A. Altomare, M. Camalli, C. Cuocci, C. Giacobozzo, A.

ARTICLE

Journal Name

- Moliterni and R. Rizzi, *J. Appl. Crystallogr.*, 2009, **42**, 1197–1202.
- 50 P. M. de Wolff, *J. Appl. Crystallogr.*, 1968, **1**, 108–113.